


Article

Microstructure and Mechanical Properties of Friction Stir Welded Joint of an Aluminum Alloy Sheet 6005A-T4

Xiaofei Sheng^{1,2,3,4} , Kai Li^{5,6}, Wenke Wu^{5,6}, Yong Yang^{5,6}, Yu Liu^{5,6}, Yifan Zhao^{5,6} and Guoai He^{5,6,*}

¹ School of Materials Science and Engineering, Hubei University of Automotive Technology, Shiyan 442002, China; auden1@126.com

² School of Materials Science and Engineering, Central South University, Changsha 410083, China

³ Key Laboratory of Automotive Power Train and Electronics (Hubei University of Automotive Technology), Shiyan 442002, China

⁴ Key Laboratory of Nonferrous Metal Materials Science and Engineering, Ministry of Education, Central South University, Changsha 410083, China

⁵ Light Alloy Research Institute, Central South University, Changsha 410083, China; lk193812055@csu.edu.cn (K.L.); ww193812041@csu.edu.cn (W.W.); 193812017@csu.edu.cn (Y.Y.); 193812035@csu.edu.cn (Y.L.); 183812035@csu.edu.cn (Y.Z.)

⁶ State Key Laboratory of High Performance Complex Manufacturing, Central South University, Changsha 410083, China

* Correspondence: heguoai@csu.edu.cn

Received: 12 October 2019; Accepted: 25 October 2019; Published: 27 October 2019



Abstract: The 6005A-T6 alloy had been widely applied in rail transmit industry due to its combination properties of moderate strength, superior resistance to corrosion, and excellent extrusion plasticity. However, few reports were related to the 6005A-T4 alloy in spite of it also presenting considerable properties. In this work, we introduced the FSW method to investigate the weldability and mechanical properties of a thin plate aluminum 6005A-T4 to evaluate its potential application. Fully recrystallized microstructure was obtained in the nugget zone, characterized by equiaxed grain with a size of 2.2 μm under current welding parameters. The tensile strength can reach as high as 174 ± 2 MPa with the absence of β phase, which is equivalent to 83.8% of that of base metal. The dissolution of β phase will dramatically reduce the micro-indentation hardness down to as low as 58 HV0.2 and the fine grain, for example 2 μm in this work, will reversely raise this value up to 64 HV0.2. Our investigation provides some perspectives to understand weldability, mechanical properties of the 6005A-T4 alloy, and develop its further applications in the related field.

Keywords: 6005A-T4 aluminum alloy; friction stir welding; recrystallization; microstructure; mechanical property; friction weldability

1. Introduction

Applying the aluminum-made coach into high speed rail train, metro, and light rail train is the principle pathway to realize the light weight of rail transmit [1,2]. The in-service conditions required by the coach possess combined performances of high strength and superior resistance to corrosion. Among the heat treatable aluminum alloy, Al-Mg-Si alloy is the exclusive one that presents most excellent performance to resistance of stress corrosion cracking. For the Al-Mg-Si alloy with the addition of Cu content, the Beta-Phase is the final equilibrium phase of Al-Mg-Si-Cu alloy, which presents as a FCC structure of CaF_2 type with chemical composition of Mg_2Si and lattice parameters of $a = 0.635$ nm,

$c = 0.405$ nm [3]. It was reported that for the Al-Mg-Si-Cu alloy with low Cu content (0.1 wt%), the precipitate sequences were found to be: SSSS→GP zones→ β'' → β' + Q' → β + Si when it was subjected to artificial ageing (usually with ageing temperature higher than 100 °C) [4]. While for the spontaneous aging, the β'' was not able to precipitate from matrix owing to the formation of GP zone in the early period which leads to decreased concentration of solute atom and vacancy. As a result, the equilibrium phase of β + Si was gradually formed in the final. Among the Al-Mg-Si-Cu alloy, it was reported that the 6005A alloy had been widely applied in the rail transmit industry due to its combination properties of moderate strength, superior resistance to corrosion, and excellent extrusion plasticity [5–7]. With the above advancing characteristics, thin-walled and hollow-core profiles with complex sections are able to be extruded for applications. In addition, the profiles can be subjected to forced air cooling right after extrusion to ensure the required microstructure. After which, welding is employed to join the individual parts into the integrated one during manufacturing of the coach. Therefore, the weldability of the alloy is particularly important. Therefore, the solid-state welding method, friction stir welding, invented in 1991, was widespread employed for aluminum welding owing to its abilities to overcome the mentioned-above disadvantages [8–13]. The hybrid technique [14,15], recrystallization mechanisms [16–18], residual stresses [19–24], crack growth behavior [25,26], corrosion susceptibility [27], during friction stir welding has been the focus.

With the help of development of the FSW technique, numerous aluminum alloys with different heat treatment status were allowed be welded to obtain considerable properties, usually with welding factor larger than 0.7. Generally, during the FSW process, severe plastic deformation occurred in the nugget zone (NZ), which would trigger the occurrence of dynamic recrystallization with sufficient heat put in, resulting in the refinement of grain size. As a result, the strength of NZ was correspondingly enhanced. However, for 6xxx aluminum alloy, most research were focused on the T6 heat treatment status [7,22,28–36] and few reports on the other status can be referred. According to our pre-research, the aluminum 6005A-T4 presented favorable performance with protentional application to automobile and rail transmit field but the welding routines and corresponding parameters remained to be unknown and need further investigation. In this work, we introduced FSW method to investigate the weldability of a thin plate aluminum 6005A-T4. The precipitation behaviors, microstructure evolution along with welding properties of the FSW welded joint were multi-scale characterized. The beta phase behaviors and recrystallization served the primary roles in affecting the properties of different welding characteristic area. The area fraction of beta phase was observed to decrease from the base metal towards the nugget zone, companied by the similar trend of average grain size. The tensile strength reached as high as 176 MPa, which is 83.8% of base metal's strength, under the current experimental conditions. Our results provide a new perspective in developing the application of aluminum 6005A-T4 and will attract board interests from researchers of automobile and rail transmit field.

2. Materials and Methods

2.1. Materials

The material used in this work was a thickness of 2 mm aluminum plate 6005A-T4 with nominal composition listed in Table 1, whose physical properties are: Density of 2700 kg/m³, thermal conductivity of 201 W/m·K, electrical conductivity of 49% ICAS. The tensile strength of parent metal with current status was determined as 208 MPa with average elongation of 12.5%.

Table 1. The nominal composition of 6005A.

Element	Mg	Si	Cu	Mn	Cr	Ti	Zn	Al
wt%	0.65	0.73	0.13	0.31	0.16	≤0.10	≤0.10	balance

2.2. Friction Stir Welding Process

The FSW tool with a diameter of 2 mm was used, schematic illustration of which was shown in Figure 1. Two plates with similar length were washed and polished to ensure the cleanliness and smoothness of sections before welding. After that, the two plates were mounted firmly on the workbench to avoid any horizontal movement during welding. The rotating speed of the tool was selected as 2100 RPM accompanied with welding speed of 100 mm/min according to our previous investigations.

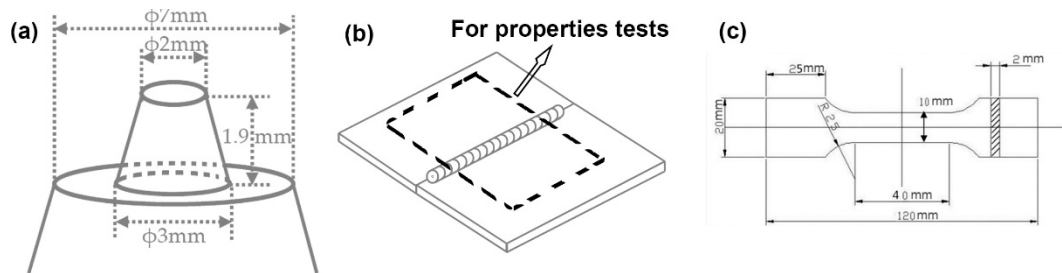


Figure 1. Schematic illustration of (a) dimensions of the FSW (Friction Stir Welding) tool and (b) samples extraction from the plate for properties tests, and (c) corresponding dimensions.

2.3. Properties Testing

The tensile tests were conducted on a MTS 810 material testing machine (MTS Systems Corporation, Eden Prairie, MN, USA) with a stretching velocity of 2 mm/min under the guide line of ASTM B209-2004. To reduce the error, at least five samples were tested for each testing condition. The HV-5 Vickers hardness tester (Laizhou Huayin Testing Instrument Co., Ltd., Laizhou, China) was employed for microindentation hardness testing. The load was set as 0.2 kg and dwell for 10 s based on the instruction of ASTM E384-2017 standard. Points with distance of 0.25 mm apart from each other were tested. Similar to the tensile tests, five samples were used and the scope of errors was controlled with ± 0.5 .

2.4. Microstructure Characterization

A field emission scanning electron microscopy (SEM, FEI Quanta 650 scanning electron microscopy, FEI Company, Hillsboro, OR), equipped with electron back scattering diffraction (EBSD, EDAX Inc., XM4-Hikari), was used for grain and fracture observations. For EBSD examinations, all the samples were prepared using metallography standard procedures under the guideline of ASTM E3-11 standard. After that, the samples were vibrating polished in solution of 30 nm colloidal silica for 4–8 h. For EBSD data collections, a step size of 0.2–0.4 μm was used to guarantee enough pixels and resolution under an acceleration voltage of 20 kV and spot size of 5.0. For TEM detections, the sample was artificially grinded to a thickness of 0.07–0.08 mm followed by being punched out to foils with 3 mm in diameter. After that, the discs were twin-jet electropolished in a solution of nitric acid and methanol (3:7 in volume fraction) at the temperature of -25 – -30° and voltage ranging from 12 V to 15 V. High resolution microstructure examinations were carried out on a field emission transmission electron microscopy (FEI Tecnai G2 F20 transmission electron microscope, FEI Company, Hillsboro, OR, USA) with an accelerating voltage of 200 kV.

3. Results

3.1. Microstructure Characterization

The microstructure of the FSW welded joints (corresponding to different welding characteristic area) and base metal (BM) obtained from EBSD, is shown in Figure 2. Figure 2a demonstrates the initial microstructure of the base metal, wherein, rod-like shape grains with some small-size ($<10 \mu\text{m}$) grains can be clearly observed. The grains were stretched along the extrusion direction and undergone severe plastic deformation, during which the process, dynamic recrystallization occurred, resulting in

formation of new grains with small size surrounding the rod-like ones. After friction stir welding, several distinct FSW welded characteristic area, nugget zone (NZ), thermo-mechanically affected zone (TMAZ), and heat affected zone (HAZ), were formed. Figure 2b presents the inverse pole figure (IPF) of HAZ, in which a larger fraction of grains with size under 10 μm were obviously detected as compared to that of BM. During FSW process, the HAZ was heated by the friction heat, which can raise the temperature up to the level of grain growth or recrystallization one in some situations. As a result, the grain growth or static recrystallization would occur in the HAZ during FWS due to the residual deformation and the sufficient heat. As for TMAZ, both deformation and temperature rise would exist, leading to the partial occurrence of dynamic recrystallization (DRX). As in the NZ, the alloy was friction stir welded and severe plastic deformation occurred in this zone, leading to the occurrence of dynamic recrystallization (DRX) and refining of the grain size to some extent [6,13,16].

As in this work, for the microstructure of HAZ, it can be observed that the size of grain was a little larger than that of BM. In the HAZ, the temperature was raised due to the friction heat, which lead to the grain growth occurring. The residual deformation energy of hot extrusion would be also released with the activation of friction heat, which would facilitate the grain growth process. For the case of HAZ, it can be seen in Figure 2c, small fraction of new dynamic recrystallized grains is formed along the broken grains. However, the DRX for most of the grains is restrained owing to the lower temperature or insufficient deformation stored energy. In the region that is close to the NZ, the dislocation will accumulate with deformation continuing and will serve as the nucleation sites to trigger the occurrence of dynamic recrystallization once the thermal conditions are also reached. In addition, a certain fraction of grains with identical orientation are found, indicating the shear deformation, which is formed by the combined force of rotation and feeding, apparently occurred in this region. While for the region close to the HAZ, the DRX process is dramatically suppressed owing to the insufficient deformation stored energy and/or heat, where fibrous grains similar to HAZ and BM can be apparently found.

As in the NZ, equiaxed grains with average grain size of about 2.2 μm were obtained after severe plastic deformation, which provided sufficient deformation heat and kernites to facilitate the DRX process. During the friction stir welding, great amount of friction heat was produced, which would raise the temperature up to sufficiently trigger the occurrence of DRX. The alloy in the advancing side of FSW was continuously stirred and broken in the region with high temperature, where DRX process occurred and the grain size was refined. Owing to the short time for grain growth of DRXed grain, the average grain size of about 2.2 μm is finally obtained, as shown in Figure 2e,f.

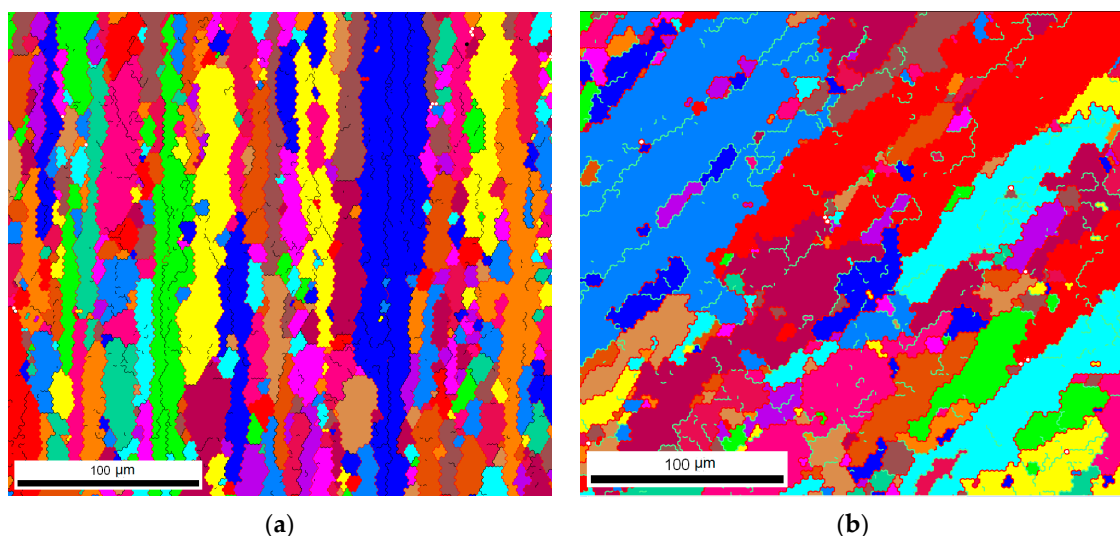


Figure 2. Cont.

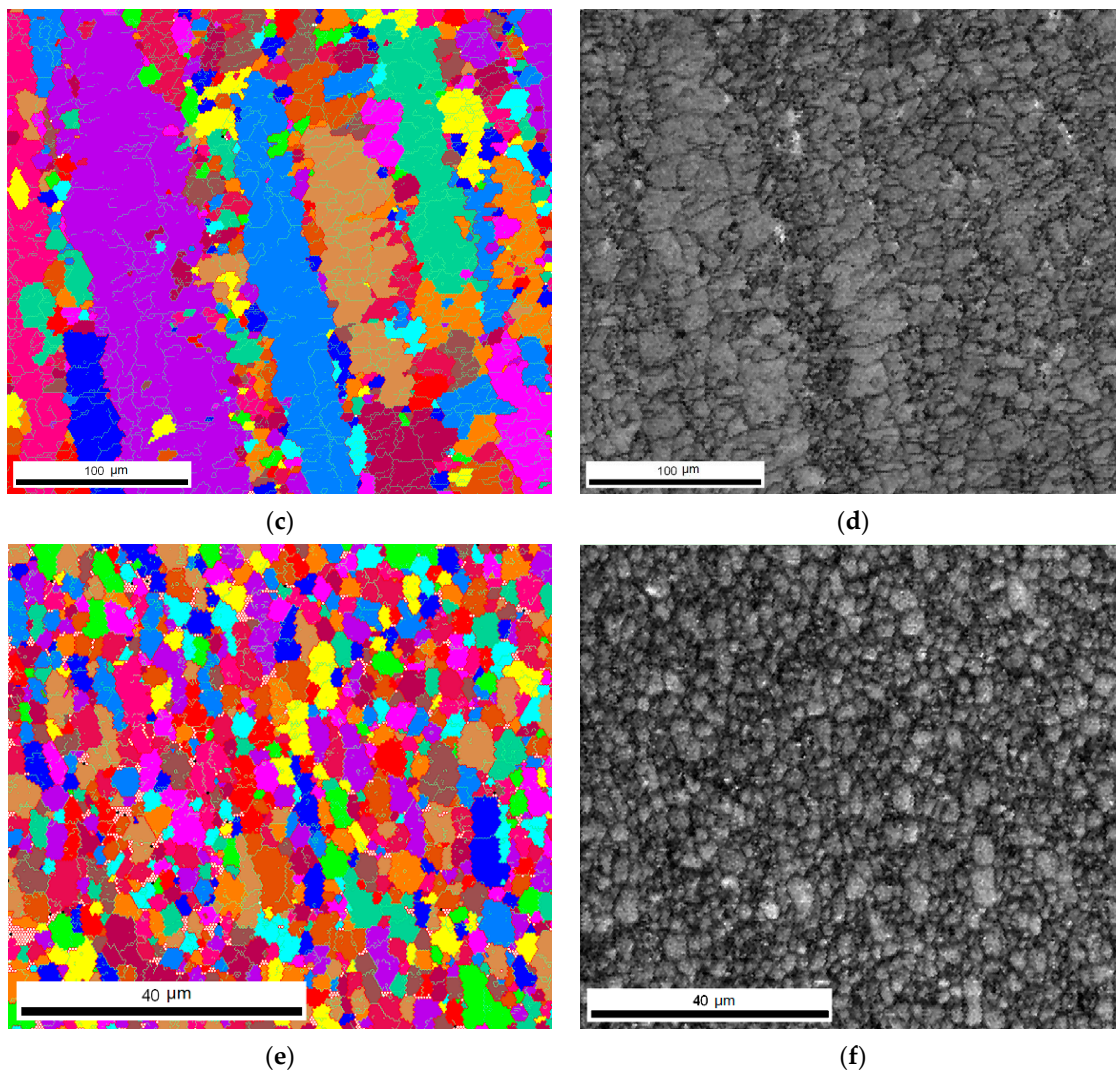


Figure 2. EBSD (Electron Back-scattering Patterns) images for different characteristic area: (a) IPF (Inverse Pole Figure) of BM (Base Metal); (b) IPF of HAZ (Heat Affected Zone); (c) and (d) IPF and back contrast image of TMAZ (Thermo-Mechanically Affected Zone), respectively; (e) and (f) IPF and back contrast image of NZ (Nugget Zone), respectively.

3.2. Precipitate Evolution

Regions of BM, HAZ, TMAZ, and NZ were examined under TEM as to reveal the precipitate evolution after FSW, results of which are shown in Figure 3. As demonstrated in Figure 3a, both strengthen phase Mg_2Si (β phase) with dimensions of 300–600 nm in length and 40–100 nm in width and undissolved phase Si are detected, distributing randomly in the matrix. The needle-shaped β phase is the primary strengthen phase for the Al-Mg-Si alloy, in which the weight ratio of Mg/Si is 1.73:1. For the 6005A alloy in this work, the weight ratio of Mg/Si is 0.89:1, which means that the amount of element Si is superfluous, resulting in the remaining of considerable amount of undissolved phase Si, as marked by the dark-solid arrows in Figure 3a. In the HAZ region, both the area fraction and size of β phase are different to the BM, as can be seen in Figure 3b. Owing to the rise of temperature, parts of β phase started to dissolve into the matrix, leading to the reduction of area fraction. In addition, due to the dissolution of β phase, the size was found to decrease to about 200–400 nm. While for the Si phase, the variations of area fraction and size were hardly distinguished because of the high dissolution temperature for Si phase. Different than the BM and HAZ, the β phase in the TMAZ were significantly dissolved into the matrix with obvious rise of temperature, resulting in the remarkable

reduction in both area fraction and size. As can be seen in Figure 3c, the size of β phase is determined to be about 200–250 nm. Similar to the behaviors of Si phase BM and HAZ, the Si phase still remained undissolved, which can be attributed to insufficient heat energy. However, the β phase are nearly dissolved and can be hardly observed in the NZ. As mentioned above, severe plastic deformation occurred in the NZ, producing high friction energy and rising the temperature to a certain degree that can substantially dissolve the β phase. Similarly, the Si phase was still detected and kept the size and fraction consistence with that of the other zones.

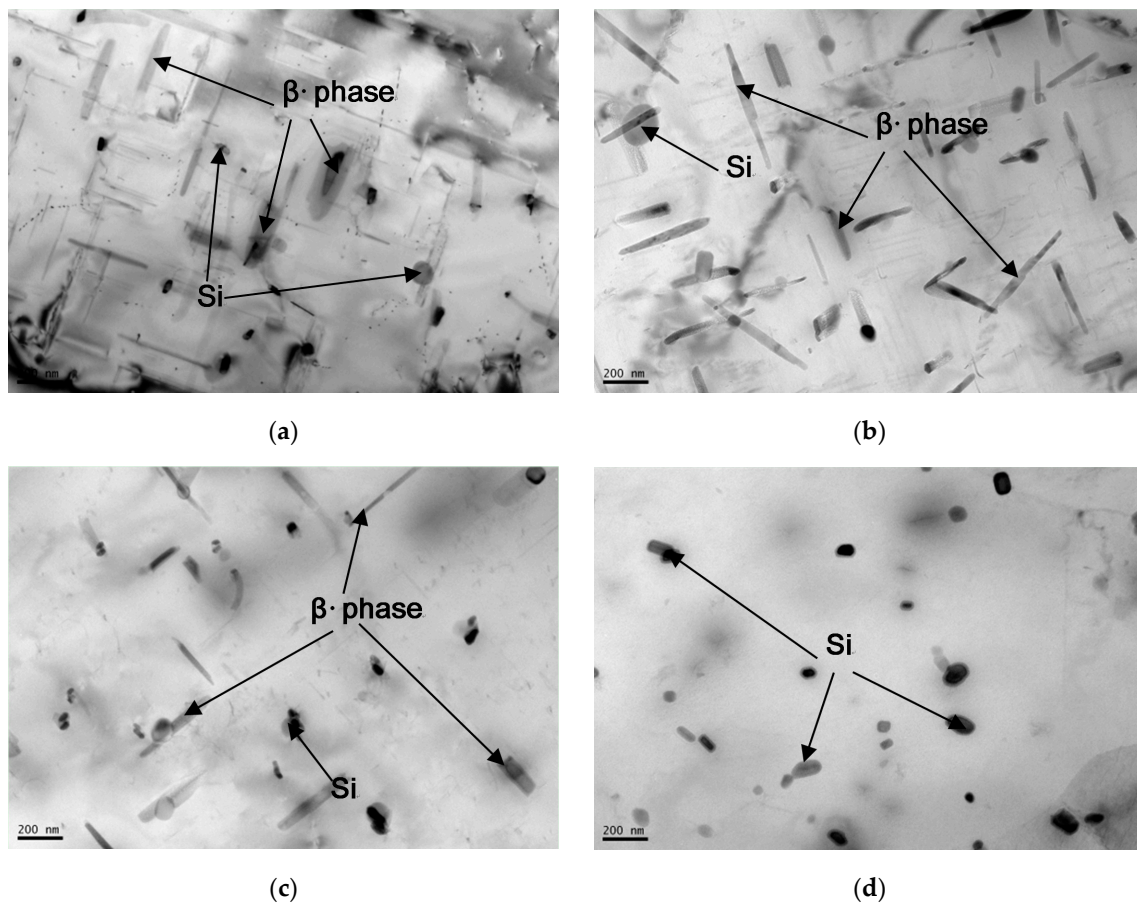


Figure 3. The TEM observations for different characteristic area showing the precipitates and second phase: (a) BM; (b) HAZ; (c) TMAZ; (d) NZ.

3.3. Tensile Property

In order to estimate the potential application, the tensile properties as well as the fracture were evaluated. Figure 4 presents the appearance of tensile specimen, which indicates that the fracture happened in the gage section. According to our tests, the average tensile strength and elongation of base metal were determined to be about 208 ± 6 MPa and $12.5\% \pm 1.2\%$, respectively. As for the welding joints, the highest tensile strength for the current alloy was 176 MPa with elongation of 8.0%, while the lowest one was 172 MPa with elongation of 9.9%. Thus, the average tensile strength and elongation of welding joints were finally calculated to be 174 ± 2 MPa and $9.0\% \pm 0.9\%$, which is equivalent to 83.8% and 79.2% of base metal ones.

For the current investigated alloy 6005A, the tensile strength was mainly controlled by the strengthening precipitate β phase and grain size. It was well documented that the nano-sized Mg_2Si usually served as obstacles to dislocations movement, which would enhance the strength of the alloy [37]. In this work, considerable fraction of nano-sized Mg_2Si with dimensions of 300–600 nm in length and 40–100 nm were obtained in the BM, as shown in Figure 3. When the BM was friction-stir

welded, friction heat would be produced and accumulated to nearly dissolve all the β phase in the NZ owing to the severe deformation according to the above analyses. The absence of β phase would make the NZ become the weakest part and be more inclined to suffer fracture if we only consider the precipitate strengthening effect. However, it should be pointed out that, the grain size is also refined to about $2.2\ \mu\text{m}$, compared to BM (with average grain size about $20\ \mu\text{m}$) owing to the occurrence of significant DRX. The micro-sized grains would increase numerous grain boundaries as compared to the BM and enhance the strength to a certain degree according to the Hall-Patch effect, compensating the lost part due to the dissolution of β phase. As a result, the average tensile strength of FSW welded joints can reach as high as $174 \pm 2\ \text{MPa}$, which is equivalent to 83.8% of that of base metal. As for comparisons, the tensile properties of 6005A-T6 FSW joints was reported to present a joint efficiency ranging between 71% and 80% in the previous work [7]. For the double-sided FSW specimen, there were good mechanical properties with a tensile strength of 80.8% of 6005A-T6 BM [22]. Moreover, the maximum tensile strength of 6005A-T6 joint at the welding speed of 400 mm/min reached 82% of base metal in another previous work [35].

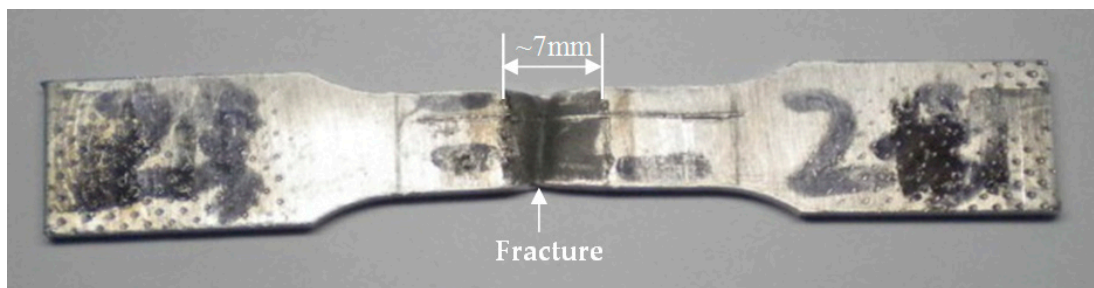


Figure 4. The appearance of FSW welded specimen after tensile test, showing the fracture was occurred in the gage section.

3.4. Microindentation Hardness Distribution in Transverse Cross-Section of the Joint

Generally, the microindentation hardness is considered as an indication of microstructure, i.e., grain and precipitate behaviors. As demonstrated in Figure 5, the variation of microindentation hardness along the length direction appears as a W-shaped profile, which is symmetrical to the NZ. As can be clearly concluded, the base metal presents a highest value of about 70 HV0.2, while the lowest value was found in the transition region between the NZ and TMAZ. From general analysis, the microindentation hardness decreased sharply in the HAZ, then decreased gradually and slowly in the TMAZ and finally increased in the NZ with distance close to the center of NZ.

It is popularly accepted that the microindentation hardness of 6005 Al alloy is closely related to grain size with micro scale and the behaviors strengthening precipitates [37]. As previous works stated that dissolution or over-aging of the strengthening precipitates under high temperature would soften the material to some degree [37]. In this work, the microindentation hardness of 6005A was primarily dominated by the distribution and numbers of strengthening precipitate β phase considering the grain size is larger than $10\ \mu\text{m}$ for most situations. As can be seen in Figure 5, large fraction of β phase Mg_2Si was detected in the BM, which makes the it present the highest value of 70 HV0.2. With the rising of temperature, most of the remained dislocation and parts of β phase Mg_2Si started to dissolved into the matrix, while in the meantime, the grain size kept consistence with BZ, leading to the dramatical drop of microindentation hardness. As in the TMAZ, the recrystallization process was triggered and parts of new fine grain started to show up due to the higher temperature and meanwhile the deformation occurred, which would slow down the drop of microindentation hardness, as can be seen in Figure 5. However, in the NZ, the grain size was refined to as fine as $2.2\ \mu\text{m}$ due to the remarkable effects of DRX, resulting in a sharp rise of microindentation hardness. As a result, the lowest microindentation hardness was observed in the transition region between TMAZ and NZ, where the grain size were large and the β phase Mg_2Si nearly dissolved.

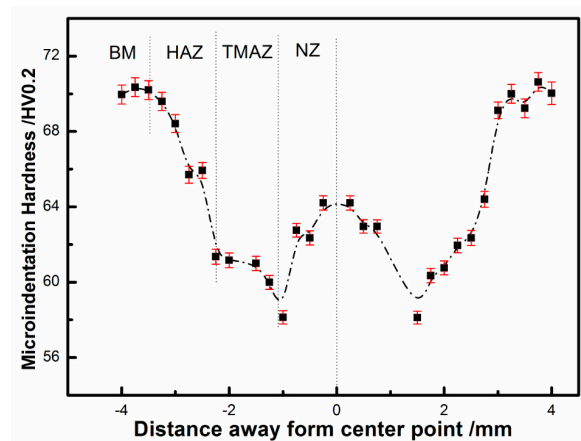


Figure 5. Variation of microindentation hardness along the length direction, resending a W-shaped profile which is symmetrical to the NZ.

3.5. Fracture Observation

To further investigate the fracture mechanisms, fracture surfaces after tensile tests were examined. Figure 6 shows the fracture morphology of base metal and FSW welded joint obtained by SEM. As can be clearly observed in Figure 6a, ellipsoid-shaped dimples were apparently found in the fracture surface of base metal, which was characterized with numerous elongated and ductility dimples with large dimension and depth as well the absence of obvious cracks. This indicates that the microvoid coalescence fracture occurred during the fracture, which showed superior plasticity of base metal. The binding force between the grains would be improved after the hot extrusion owing to the effects of severe plastic deformation and high temperature. No brittle particles with large size was produced during the hot extrusion and subsequent spontaneous ageing, as shown in Figure 6a, which also improve the plasticity of the base metal.

As for the fracture of the FSW welded joint, small-sized dimples with a relatively shallow depth compared to that of base metal were clearly presented. During the FSW process, the grains in the NZ were dramatically broken and recombined in a relatively low temperature compared to the hot extrusion one, which would lead to the drop of binding force between the grains. For another aspect, the residual stress would be raised due to the severe plastic deformation during FSW and rapid cooling after FSW, which would also lower the plasticity of FSW welded joint. From the above characteristics of fracture surface, the plasticity of the base metal is better than that of FSW welded alloy, which is consistent with the results of tensile test, as shown in Section 3.3.

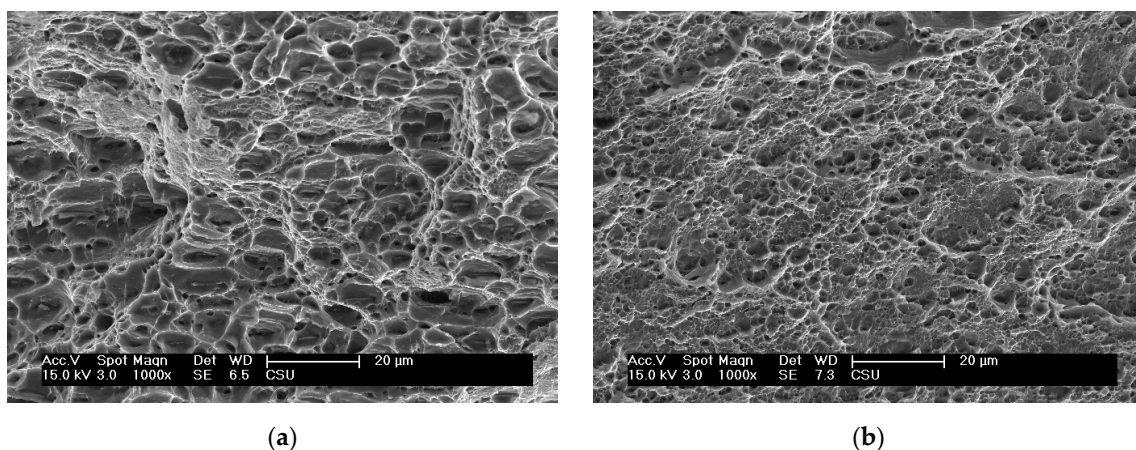


Figure 6. The fracture morphology of the base metal (a) and FSW welded joint obtained (b) by SEM.

4. Conclusions

In this article, the solid-state process, friction stir welding, was employed to study weldability and mechanical properties of a thin plate aluminum 6005A-T4 and thus evaluate corresponding potential application in automobile and rail transmit field. Based on the above analyses on the current alloy 6005A-T4, fully recrystallized microstructure was obtained in the nugget zone, characterized by equiaxed grains with average size of 2.2 μm under current welding parameters. The tensile strength can reach as high as 174 ± 2 MPa with the absence of β phase, which is equivalent to 83.8% of that of the base metal. The microindentation hardness was dominated by the strengthening precipitate in the FSW welded joint and affected significantly by very fine grain size. The dissolution of β phase will dramatically reduce the microindentation hardness down to as low as 58 HV0.2 and the fine grain, for example 2 μm in this work, will reversely raise this value up to 64 HV0.2. It should be noted that the current parameters are not the optimal ones and not directly related to the application of this alloy 6005A-T4 but should provide some perspectives to understand weldability and develop its further applications in the related field.

Author Contributions: Conceptualization, X.S.; Methodology, X.S. and G.H.; Investigation, K.L., W.W., Y.Y., Y.L., and Y.Z.; Data curation, X.S.; Writing—original draft preparation, X.S.; Writing—review and editing, G.H.; Visualization, Y.Z.; Supervision, G.H.; Funding acquisition, G.H.

Funding: The APC was funded by the Project of State Key Laboratory of High Performance Complex Manufacturing, Central South University (ZZYJKT2019-04); Scientific research initial funding of Central South University (202045001); National Natural Science Foundation of China (51901247); Research Project of Hubei Provincial Education Department (Q20191802); Doctoral Research Startup Fund in Hubei University of Automotive Technology (K201802); Hubei Provincial Natural Science Foundation of China (2020CFBXXX).

Conflicts of Interest: The authors declare no conflict of interest.

References

1. Barbieri, G.; Cognini, F.; Lapi, G.; Vivio, F. Mechanical Behavior of Aluminum Sandwiches Made by Laser Welding. *Procedia Eng.* **2015**, *109*, 427–434. [[CrossRef](#)]
2. Simar, A.; Bréchet, Y.; De Meester, B.; Denquin, A.; Pardoën, T. Microstructure, local and global mechanical properties of friction stir welds in aluminium alloy 6005A-T6. *Mater. Sci. Eng. A* **2008**, *486*, 85–95. [[CrossRef](#)]
3. Arnberg, L.; Aurivillius, B.; Ebba, W.; Gunnar, M. The crystal structure of $\text{Al}_x\text{Cu}_2\text{Mg}_{12-x}\text{Si}_7$, (h-AlCuMgSi). *Acta Chem. Scand. A* **1980**, *34*, 1–5. [[CrossRef](#)]
4. Miao, W.F.; David, E. Effects of Cu content and preaging on precipitation characteristics in Aluminum alloy 6022. *Metall. Mater. Trans. A* **2000**, *31*, 361–371. [[CrossRef](#)]
5. Hirsch, J. Aluminium Alloys for Automotive Application. *Mater. Sci. Forum* **1997**, *242*, 33–50. [[CrossRef](#)]
6. Lee, W.B.; Yeon, Y.M.; Jung, S.B. Evaluation of the microstructure and mechanical properties of friction stir welded 6005 aluminum alloy. *Mater. Sci. Technol.* **2003**, *19*, 1513–1518. [[CrossRef](#)]
7. Peng, D.; Hongmei, L.; Daqian, S.; Wenbiao, G.; Jie, L. Effects of welding speed on the microstructure and hardness in friction stir welding joints of 6005A-T6 aluminium alloy. *Mater. Des.* **2013**, *45*, 524–531.
8. Thomas, W.M.; Nicholas, E.D.; Needham, J.C. Friction Stir Butt Welding: International patent application No. PCT/GB92102203 and Great Britain Patent. Application No.9125978.8[P], 6 December 1991.
9. Threadgill, P.L.; Leonard, A.J.; Shercli, H.R.; Withers, P.J. Friction stir welding of aluminium alloys. *Int. Mater. Rev.* **2009**, *54*, 49–93. [[CrossRef](#)]
10. Shi, Y.; Tang, W. The principle and application of the friction stir welding. *Welding* **2000**, *30*, 6–9.
11. Ping, Y.; Peng, H. Current status and developing tendency of Friction Stir Welding. *Foreign Locomot. Roll. Stock Technol.* **2004**, *1*, 65–69.
12. Ma, H.; Wang, Y.; Tian, Z.; Xiong, L.; Zhang, Y. Gap-tolerance control for friction stir butt welding of 2A14 aluminium alloy. *Measurement* **2019**, *148*, 106915. [[CrossRef](#)]
13. Hassan, K.A.; Prangnell, P.B.; Norman, A.F.; Price, D.A.; Williams, S.W. Effect of welding parameters on nugget zone microstructure and properties in high strength aluminium alloy friction stir welds. *Sci. Technol. Weld. Join.* **2003**, *8*, 257–268. [[CrossRef](#)]

14. Citarella, R.; Carlone, P.; Lepore, M.A.; Sepe, R. Hybrid technique to assess the fatigue performance of multiple cracked FSW joints. *Eng. Fract. Mech.* **2016**, *162*, 38–50. [[CrossRef](#)]
15. Patel, V.; Li, W.; Wang, G.; Wang, F.; Vairis, A.; Niu, P. Friction Stir Welding of Dissimilar Aluminum Alloy Combinations: State-of-the-Art. *Metals* **2019**, *9*, 270. [[CrossRef](#)]
16. Mcnelley, T.R.; Swaminathan, S.; Su, J. Recrystallization mechanisms during friction stir welding/processing of aluminum alloys. *Scr. Mater.* **2008**, *58*, 349–354. [[CrossRef](#)]
17. Sauvage, X.; Dede, A.; Cabello, A. Precipitate stability and recrystallisation in the weld nuggets of friction stir welded Al-Mg-Si and Al-Mg-Sc alloys. *Mater. Sci. Eng. A* **2008**, *491*, 364–371. [[CrossRef](#)]
18. Tao, W.; Yong, Z.; Xuemei, L.; Matsuda, K. Special grain boundaries in the nugget zone of friction stir welded AA6061-T6 under various welding parameters. *Mater. Sci. Eng. A* **2016**, *671*, 7–16. [[CrossRef](#)]
19. Haghshenas, M.; Gharghoury, M.A.; Bhakhri, V.; Klassen, R.J.; Gerlich, A.P. Assessing residual stresses in friction stir welding: Neutron diffraction and nanoindentation methods. *Int. J. Adv. Manuf. Technol.* **2017**, *93*, 3733–3747. [[CrossRef](#)]
20. Xu, W.; Liu, J.; Zhu, H. Analysis of residual stresses in thick aluminum friction welded butt joints. *Mater. Des.* **2011**, *32*, 2000–2005. [[CrossRef](#)]
21. Deplus, K.; Simar, A.; Van Haver, W.; De Meester, B. Residual stresses in aluminium alloy friction stir welds. *Int. J. Adv. Manuf. Technol.* **2011**, *56*, 493–504. [[CrossRef](#)]
22. Liu, X.; Xie, P.; Wimpory, R.; Li, W.; Lai, R.; Li, M.; Chen, D.; Liu, Y.; Zhao, H. Residual Stress, Microstructure and Mechanical Properties in Thick 6005A-T6 Aluminium Alloy Friction Stir Welds. *Metals* **2019**, *9*, 803. [[CrossRef](#)]
23. Woo, W.; Feng, Z.; Wang, X.L.; David, S. Neutron diffraction measurements of residual stresses in friction stir welding: A review. *Sci. Technol. Weld. Join.* **2011**, *16*, 23–32. [[CrossRef](#)]
24. Prime, M.; Gnaupel-Herold, T.; Baumann, J.; Lederich, R.; Bowden, D.; Sebring, R. Residual stress measurements in a thick, dissimilar aluminum alloy friction stir weld. *Acta Mater.* **2006**, *54*, 4013–4021. [[CrossRef](#)]
25. Sepe, R.; Armentani, E.; Di Lascio, P.; Citarella, R. Crack Growth Behavior of Welded Stiffened Panel. *Procedia Eng.* **2015**, *109*, 473–483. [[CrossRef](#)]
26. Citarella, R.; Carlone, P.; Sepe, R.; Lepore, M.A. DBEM crack propagation in friction stir welded aluminum joints. *Adv. Eng. Softw.* **2016**, *101*, 50–59. [[CrossRef](#)]
27. Dong, P.; Sun, D.; Wang, B.; Zhang, Y.; Li, H. Microstructure, microhardness and corrosion susceptibility of friction stir welded AlMgSiCu alloy. *Mater. Des.* **2013**, *54*, 760–765. [[CrossRef](#)]
28. Malopheyev, S.; Vysotskiy, I.; Kulitskiy, V.; Mironov, S.; Kaibyshev, R. Optimization of processing-microstructure-properties relationship in friction-stir welded 6061-T6 aluminum alloy. *Mater. Sci. Eng. A* **2016**, *662*, 136–143. [[CrossRef](#)]
29. Simar, A.; Bréchet, Y.; De Meester, B.; Denquin, A.; Gallais, C.; Pardoën, T. Integrated modeling of friction stir welding of 6xxx series Al alloys: Process, microstructure and properties. *Prog. Mater. Sci.* **2012**, *57*, 95–183. [[CrossRef](#)]
30. Feng, Z.; Wang, X.L.; David, S.A.; Sklad, P.S. Modeling of residual stresses and property distributions in friction stir welds of aluminum alloy 6061-T6. *Sci. Technol. Weld. Join.* **2013**, *12*, 348–356. [[CrossRef](#)]
31. Fadaeifard, F.; Matori, K.A.; Aziz, S.A.; Zolkarnain, L.; Rahim, M.A.Z.B.A.; Rahim, M.A. Effect of the Welding Speed on the Macrostructure, Microstructure and Mechanical Properties of AA6061-T6 Friction Stir Butt Welds. *Metals* **2017**, *7*, 48. [[CrossRef](#)]
32. Sakala, R.S.; Renangi, S.; Indira, R.M. Experimental study of double sided friction stir welding of AA 6061 plates using hexagonal tool tip. *Int. J. Res. Advent Technol.* **2018**, *6*, 32–37.
33. Woo, W.; Feng, Z.; Wang, X.L.; Brown, D.W.; Clausen, B.; An, K.; Choo, H.; Hubbard, C.R.; David, S.A. In situ neutron diffraction measurements of temperature and stresses during friction stir welding of 6061-T6 aluminium alloy. *Sci. Technol. Weld. Join.* **2007**, *12*, 298–303. [[CrossRef](#)]
34. Li, S.; Chen, Y.; Kang, J.; Amirkhiz, B.S.; Nadeau, F. Effect of Revolutionary Pitch on Interface Microstructure and Mechanical Behavior of Friction Stir Lap Welds of AA6082-T6 to Galvanized DP800. *Metals* **2018**, *8*, 925. [[CrossRef](#)]
35. Ji, S.D.; Meng, X.C.; Liu, J.G.; Gao, S.S. Formation and mechanical properties of stationary shoulder friction stir welded 6005A-T6 aluminum alloy. *Mater. Des.* **2014**, *62*, 113–117. [[CrossRef](#)]

36. Simar, A.; Bréchet, Y.; De Meester, B.; Denquin, A.; Pardoën, T. Sequential modeling of local precipitation, strength and strain hardening in friction stir welds of an aluminum alloy 6005A-T6. *Acta Mater.* **2007**, *55*, 6133–6143. [[CrossRef](#)]
37. Yang, W.; Wang, M.; Sheng, X.; Zhang, Q.; Huang, L. Precipitate characteristics and selected area diffraction patterns of the β' and Q' precipitates in Al–Mg–Si–Cu alloys. *Philos. Mag. Lett.* **2011**, *91*, 150–160. [[CrossRef](#)]



© 2019 by the authors. Licensee MDPI, Basel, Switzerland. This article is an open access article distributed under the terms and conditions of the Creative Commons Attribution (CC BY) license (<http://creativecommons.org/licenses/by/4.0/>).